

Article

Surface Characteristics of Machined Polystyrene with 3D Printed Thermoplastic Tool

Kamalpreet Sandhu ¹, Gurminder Singh ², Sunpreet Singh ³, Raman Kumar ⁴,
Chander Prakash ⁵, Seeram Ramakrishna ³, Grzegorz Królczyk ⁶ and Catalin I. Pruncu ^{7,8,*}

¹ Department of Product and Industrial Design, Lovely Professional University, Phagwara 144411, India; Kamalpreet.23686@lpu.co.in

² Science et Ingénierie des Matériaux et Procédés (SIMAP), Université Grenoble Alpes, 38400 Grenoble, France; Gurminder.singh@grenoble-inp.fr

³ Mechanical Engineering, National University of Singapore, Singapore 117584, Singapore; snprt.singh@gmail.com (S.S.); seeram@nus.edu.sg (S.R.)

⁴ Department of Mechanical Engineering, Guru Nanak Dev Engineering College, Ludhiana 141006, India; sehgal91@gndec.ac.in

⁵ School of Mechanical Engineering, Lovely Professional University, Phagwara 144411, India; chander.21503@lpu.co.in

⁶ School of Mechanical Engineering, Opole University, 45-758 Opole, Poland; g.krolczyk@po.opole.pl

⁷ Department of Mechanical Engineering, Imperial College London, Exhibition Rd., London SW7 2AZ, UK

⁸ Department of Mechanical Engineering, School of Engineering, University of Birmingham, Birmingham B15 2TT, UK

* Correspondence: c.pruncu@imperial.ac.uk

Received: 6 May 2020; Accepted: 12 June 2020; Published: 16 June 2020



Abstract: An effort is made in this work to appraise the surface characteristics of machined expandable polystyrene (EPS) with a novel 3D printed thermoplastic acrylonitrile-butadiene-styrene (ABS) tool. Linear grooves on EPS were made on a vertical milling machine that was modified to conduct experiments in the laboratory. The tests were designed as per the Taguchi L9 based factorial design of experimentation while varying process parameters such as depth of cut, spindle speed, and feed rate. The machining responses dimensional accuracy and surface roughness of the machined grooves were studied. Furthermore, the surface topography of the machined specimens was considered to investigate the mechanism of material removal in response to the processing conditions. Moreover, mathematical models developed for the prediction of the output responses showed a significant correlation with the experimental results. The results of the statistical study indicate that the surface roughness is influenced by the spindle speed and dimensional accuracy by the depth-of-cut. Overall, the findings of the experimental work advocated the feasibility of 3D printed thermoplastic tools for machining soft polymeric materials. It can become a useful alternative for mass and batch production.

Keywords: three-dimensional printing; fused deposition modelling; dimension accuracy; surface roughness; milling; expandable polystyrene; thermoplastic tool

1. Introduction

In today's competitive world, industries are rigorously spotlighting on essential aspects such as time, quality, and cost of products to manage the immense pressure [1]. As the need for sustainable manufacturing increases [2], researchers have started to explore the various processes which can deliver the desired outcomes as compared to traditional production activities like machining or injection moulding, while taking care of environmental perspectives [3,4]. However, the three-dimensional (3D) printing methods are often explicit with their specific feedstock materials as compared to conventional

manufacturing [5]. Indeed, in the 3D printing technologies, a robust computerized model is used as input design, which results in the saving of material [6]. Since the invention of 3D printing technologies in the 1980s, the pace has gradually shifted from prototyping to rapid manufacturing while growing its customization level [7]. Moreover, in today's manufacturing scenario where the design of the industrial products changes very often, owing to the change in the lifestyle of the customers, 3D printing technology is the only available option that can cope with sudden design changes quickly and cost-effectively [8]. Furthermore, the continuous technological innovations in 3D printing technologies have set a new paradigm wherein the printed products are being used for the end-user functional and non-functional applications [9,10]. It was observed that amongst different types of 3D printing technologies, fused deposition modelling (FDM) served most of such applications [11,12]. FDM is a well-established technology, the working principle, structural schematic, and input process variables are already documented in the literature [13–15]. It was observed that the FDM system is straightforward, relatively cost-effective in terms of equipment and materials, demands less maintenance, and is widely suitable for most of the engineering polymers and their composites [16–18]. As a consequence, FDM is commonly used for the manufacture of experimental models, prototypes, and engineering components where the prints produced are exclusively the task of input process parameters [19,20]. However, on the downside, this system suffers from numerous demerit characteristics, for example, low production speed, poor surface quality, etc. [21].

Acrylonitrile-butadiene-styrene (ABS) is one of the mainly preferred commercial feedstock material; however, alternative materials could be easily fabricated [22,23]. The literature reveals that researchers have developed FDM's in-house feedstock by utilizing a range of polymer matrices [24–26] and reinforcements [27–29] to meet sophisticated requests of highly demanding end-user applications [30,31]. Furthermore, 3D printed tools are the amongst the mainly chosen industrial applications of FDM, as illustrated by Hierl et al. [32], Kumta et al. [33], Ciocca et al. [34], and Masood and Song [35]. 3D printed tools are also used for developing customized surgical guides and templates [36,37]. Additionally, the products of FDM are acceptable as sacrificial patterns for various types of casting operations [38]. In another novel application of FDM, researchers suggested that the technology has the efficiency for producing tools for grinding operations [39], bioengineering tools [40,41], automotive parts [42], load-bearing apparatus [43], drug-bearing gadgets [44], and sensors/actuators [45]. In [46,47], the authors have studied the efficiency of FDM based tools for sheet metal forming operations.

Haeberle and Desai [47] compared the performance of traditional CNC and polystyrene based thermoform tooling and found that the latter are cost-effective, with comparable quality, quicker in cutting progress time, and capable of producing yields 50% less than the former. Further, ABS was identified as one of the most economical choices to obtain customized tools for a variety of end-user applications [47]. In [48], it was highlighted that the 3D printed tooling provides an excellent alternative to conventional metallic counter parts. Masood and Song [35] developed iron particles in nylon type matrix inserts through 3D printing and obtained excellent tensile properties. Table 1 lists the various research efforts made on the machining of soft polymers.

From the literature review, it was found that minimal studies are available for producing FDM-based machining tools for soft polymeric materials, for example, polystyrene. The present study investigates the efficiency of the FDM-based ABS tool for machining expandable polystyrene (EPS). Further, ABS is a potential candidate for developing customized tooling, through 3D printing, owing to its high tensile strength, desirable hardness, wear resistance, and corrosion resistance. Linear grooves have been made on the EPS surface at variable combinations of input process variables. The effect of spindle speed, feed rate, and depth-of-cut were studied on the finally obtained samples with measured surface roughness and dimensional accuracy. The test runs were appraised through the Taguchi L9 factorial design of experimentation.

Table 1. List of machining activities on soft polymers.

| Tool Material | Machine | Material Cutting | Summary |
|---|--|----------------------------|---|
| Stainless Steel | CNC Milling Machine | Polyurethane | The researchers found that surface roughness of tested samples was significantly affected by cell size and depth-of-cut. The additive manufacturing-based tooling provided a good alternative to conventional CNC-based tooling based on its low cost and rapid turnover [48]. |
| Hot-Wire Frame Cutter | Flexible Automated System (FAS) | Polyurethane foams | The FAS significantly reduced the cutting time and improved cutting quality. It has more flexibility to handle dissimilar geometries and more advantages over molding while making foam cushions [49]. |
| Hot Wire, Water Jet, Hot Ribbon Hot Tool | Free Form Automated Sculpting Technology, True Surface System, Shape Maker, Model Angelo, Free Foam Thick-Layered Object Manufacturing, Variable Lamination Manufacturing, Rapid-Heat Ablation, Michelangelo | Polyurethane foams | The review paper described a different kind of cutting machine form. Suggested and discussed the relative merits of rapid prototype systems to enhance foam cutting systems [50]. |
| High-Speed Steel | Milling | Flexible polyurethane foam | In this work, it was observed that at spindle speed ~2400 rpm and feed rate ~2400–4000 mm/min is suitable for distortion-less geometries. It is likely to build up customized products to convince the explicit requirements of persons with disabilities [51]. |
| Hot Wire | Four Axis Automated Hotwire Cutter | Polyurethane foam | The part quality and dimensional accuracy depend on machining parameters. The work investigated the part quality and dimensional accuracy while hot cutting of foam in two different cutting angles and found that cutting parameters influenced the quality of the parts [52]. |
| Drill, Mill Cutter, Saw Cutter | Lathe, Milling, Sawing | Polyurethane foam | The work presented an excellent application of the process for orthopedics [53]. |

2. Materials and Methods

The EPS was utilized as workpiece material in the current study, and Thermo Packers, Jalandhar, India supplied it. As per the supplier's data-sheet, the EPS has a density of 30–45 kg/m³, thermal conductivity of 0.034 W/mK, molecular weight of 224 × 103, polydispersity index > 2.3 Mw/Mn, density of 1.01 g/cm³, and MFI of 10.2 g/10 min. The key reasons behind the selection of EPS in this study were: (i) it has widespread utility as a packaging material, (ii) it demands post-operations to engrave fine details through machining, (iii) it is softer and presents potential applications to use 3D printed polymeric tools while post-processing, and (iv) the presence of the voids in the EPS matrix challenges the post-processing. The CREO 4.0 software was utilized to design the end-mill cutting tool; outside ϕ of 15 mm; the number of flutes/teeth at 4; thickness of the tooth of 1 mm; flute length of 45 mm; overall length of 50 mm; and helix angle of 20°. The standard tessellation language (STL) format was used to slice using Slicer3r and STL of layer thickness 0.254 mm is attained from the CAD model. Every test model was retained to a precision of chord height of 0.0593 and an angle conversation format of 0°. After this, the tool was printed with commercially available ABS feedstock (ϕ of 1.75 mm) using the FDM system (make: Divide by Zero, Pune, India). The part infill density of 100% was utilized at 35 mm/min of speed to print the end-mill tool with orientation parallel to the bed at a raster angle of $\pm 45^\circ$. These printing parameters have been obtained from [49,50]; these maintained the minimal deviations of dimensions of the constructed tool in comparison to the CAD model, as well as producing superior surface quality. The width of 14.998 mm was obtained for the printed end-mill tool and is utilized for the next machining operations, as shown in Figure 1.



Figure 1. As-printed acrylonitrile-butadiene-styrene (ABS) end-mill tool.

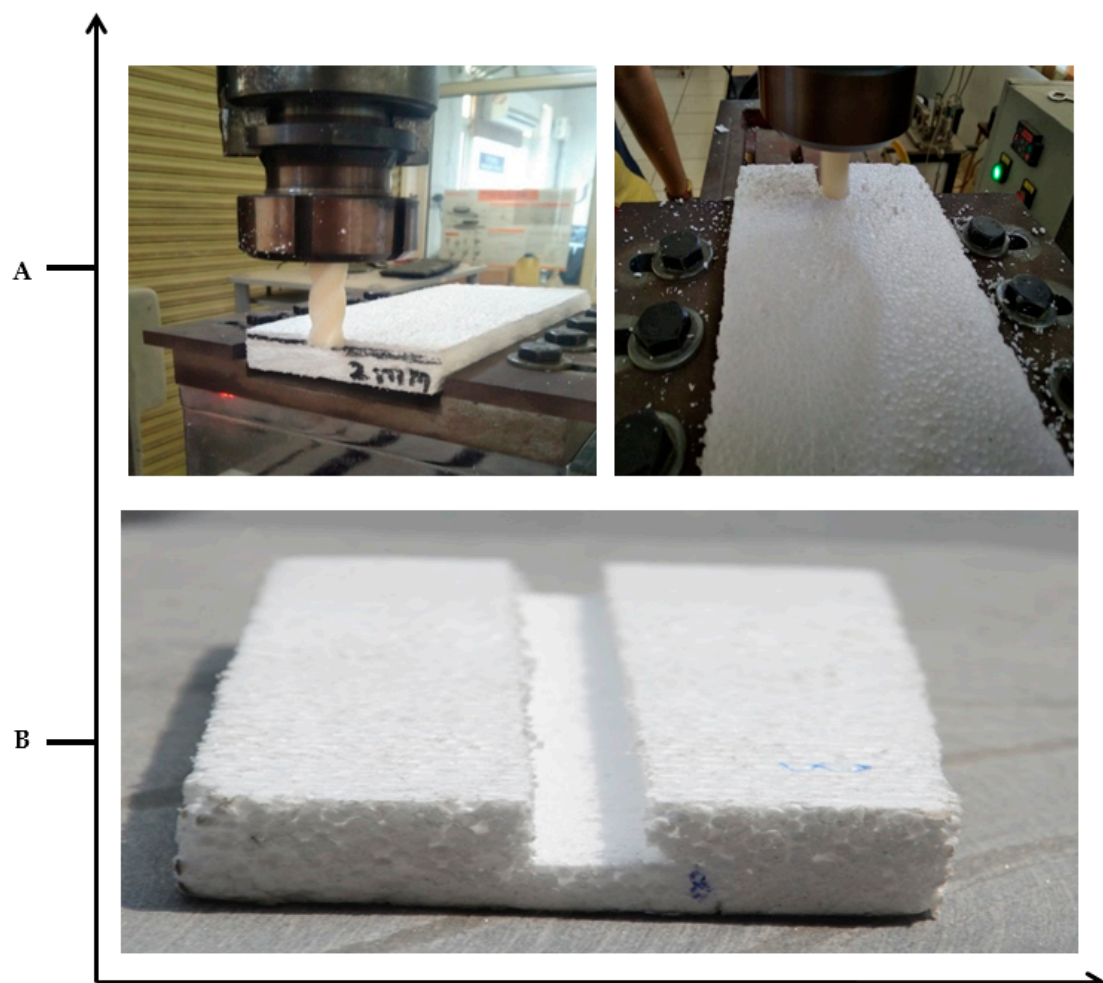
The milling machine available in the laboratory was utilized for the end milling of EPS with some modifications. The input process parameters and their levels are tabulated in Table 2. The process parameters were selected based on evidence available from the literature for surface roughness and dimensional accuracy of the end-milling operations [54,55]. Table 3 depicts the L9 standard array (the Taguchi's design of experiments) utilized to conduct the test runs. Additionally, Figure 2 shows the pictorial representations of the end-milling of the EPS utilizing the 3D printed ABS tool, which finally produced a groove. The dimensional accuracy (DA) of the subsequently machined grooves was recorded by using a coordinate measuring machine (CMM) made by Accurate Spectra, Pune, India. Two-dimensional deviations were recorded in terms of the width and depth of the cut. The raw data in this regard was obtained by subtracting the change in dimension from the set dimension and named as deviation-in-width (DIW) and deviation-in-height (DIH). In the case of DIW, DA was recorded by subtracting the size measured with CMM and the diameter of the end tool. Whereas, in the case of DID, the raw data was obtained by subtracting the cut's depth identified with CMM and the experimental value of the depth of cut (DoC).

Table 2. Selected input process parameters and their levels.

| Parameters Units S. No. | Feed Rate, F mm/min A | Spindle Speed, S rpm B | Depth of Cut, DoC mm C |
|-------------------------------|-----------------------------|------------------------------|------------------------------|
| Level 1 | 30 | 1500 | 2 |
| Level 2 | 40 | 1700 | 4 |
| Level 3 | 50 | 2000 | 6 |

Table 3. Experimentation approach based on the designed experimental log.

| Exp. No. | A | B | C |
|----------|----|------|---|
| 1 | 30 | 1500 | 2 |
| 2 | 30 | 1700 | 4 |
| 3 | 30 | 2000 | 6 |
| 4 | 40 | 1500 | 4 |
| 5 | 40 | 1700 | 6 |
| 6 | 40 | 2000 | 2 |
| 7 | 50 | 1500 | 6 |
| 8 | 50 | 1700 | 2 |
| 9 | 50 | 2000 | 4 |

**Figure 2.** Pictorial views of the end-milling of the expandable polystyrene (EPS) using: A, 3D printed tool and B, as-machined EPS.

The EPS is a soft material, and the measurement of the surface roughness with a universal stylus-based instrument might not be able to produce reliable outcomes. Therefore, in this work, a non-contact 3D optical profiler system (accuracy: 0.15 nm; make: NanoMap, NanoMap, AEP Technology, Santa Clara, CA, USA, 1000 WLI) was used to provide the average roughness value of the machined surface. Moreover, a Dino-lite microscope was utilized to capture the surface morphology of the machined parts. The microscope was calibrated by using a standard scale provided by the manufacturer. Images were captured at two different magnifications: 60× and 75×, to analyze the different machining parameters' effects on the surface morphology. The Zeta Instruments Profilometer was utilized to record the optical profiles of the machined surfaces.

3. Results and Discussion

3.1. Single Objective-Optimization

The recorded observations for DA and surface roughness (R_a) are shown in Table 4, along with signal-to-noise (S/N). The responses, such as DIW, DIH, and R_a , are “the smaller, the better” options and are optimized by using the Minitab-17 statistical software package. For a detailed description of the conversion of the raw data to the S/N ratio and plotting, the S/N ratio is well discussed elsewhere [56–58]. The main issue in this type of optimization is the difficulty in selecting the suitable input process parameters for all the considered outputs since the one optimized setting is likely to conflict with the others. On the other hand, this type of optimization is highly beneficial to get detailed insights into parametric effects as the observations are independent and free of influence from the different responses. The S/N ratio plots for DIW, DIH, and R_a are shown in Figure 3, to find the optimal parametric setting and effect of diverse variables. Figure 3 clearly depicts that in the case of DIW, the dimensional accuracy of the cut increases when the feed rate increases from 30 to 40 mm/min, and then further from 40 mm/min to 50 mm/min. This is mainly because, at a higher level of the feed rate, the time spent by the cutting tool in machining the groove was least. Therefore, the tool passed quickly across the cutting groove without causing thermal shocks to the work material. It was found that the EPS is highly thermal sensitive, and its structure consists of micro-balls that tend to squeeze upon thermal stimulus.

Table 4. Observed results for deviation-in-width (DIW), deviation-in-height (DIH), and surface roughness (R_a).

| S. No. | Deviation-In-Width, DIW (mm) | S/N Ratio (dB) | Deviation-In-Height, DIH (mm) | S/N Ratio (dB) | Surface Roughness, R_a (μm) | S/N Ratio (dB) |
|-----------------------|------------------------------|----------------|-------------------------------|----------------|--|----------------|
| 1 | 1.45 | −3.227 | 2.55 | −8.130 | 13.02 | −22.2982 |
| 2 | 1.27 | −2.076 | 2.21 | −6.887 | 11.52 | −21.2298 |
| 3 | 1.01 | −0.086 | 2.47 | −7.853 | 9.01 | −19.0964 |
| 4 | 1.25 | −1.938 | 2.33 | −7.347 | 10.56 | −20.4799 |
| 5 | 1.05 | −0.423 | 2.32 | −7.309 | 9.08 | −19.1636 |
| 6 | 0.77 | 2.2702 | 1.97 | −5.889 | 9.11 | −19.1980 |
| 7 | 0.98 | 0.1755 | 2.08 | −6.361 | 6.02 | −15.5991 |
| 8 | 0.56 | 5.0362 | 1.18 | −1.437 | 5.01 | −14.0002 |
| 9 | 0.38 | 8.4043 | 1.16 | −1.289 | 4.12 | −12.3043 |
| Overall S/N ratio, dB | - | 0.904 | - | −5.833 | - | −18.15 |

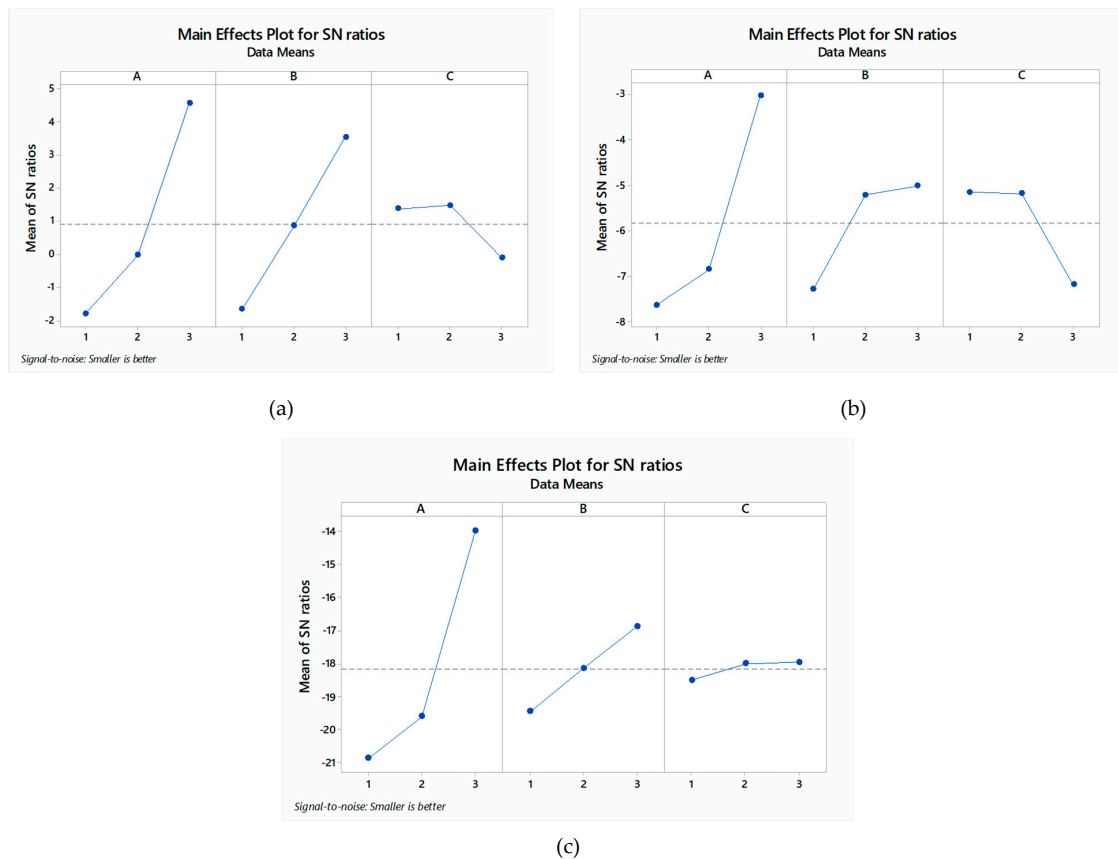


Figure 3. S/N ratio plots for DIW (a), DIH (b), and R_a (c). Note: A, B, and C represent feed rate, spindle speed, and depth-of-cut, respectively.

The feed rate of the end-mill operation, in the present case, defines the magnitude of machining heat propagating through the work material. Therefore, the fast pass of the end-mill tool secures the work material from in-process heat production. As a result, the DIW feature of the as-machined was improved by increasing the feed rate to 50 mm/min. It is worth mentioning that interconnected micro-balls of EPS possess less bond strength. Hence, a low feed rate of the end-mill tool can cause dimensional deviations. Figure 4 shows (a) the effect of in-process thermal-stimulus originated squeezing and (b) dislocation of the micro-balls on the morphology of machined-EPS, at low feed rate. Whereas, Figure 4c shows the machined surface at 50 mm/min with no visible machining incurred surface defects. In the case of spindle speed, it can be seen from Figure 3 that the DIW is improved by increasing the spindle speed. The spindle speed in machining represents the cutting force applied to the work material. While machining EPS, it was observed that as the spindle speed was increased, the end-milling tool exerted greater force on the work material and imparted the brittle fractures. That usually happens in a fraction of seconds and leaves no room for the work material to produce abrupt cutting behaviors, for example pulling or dislocation of the micro-balls.

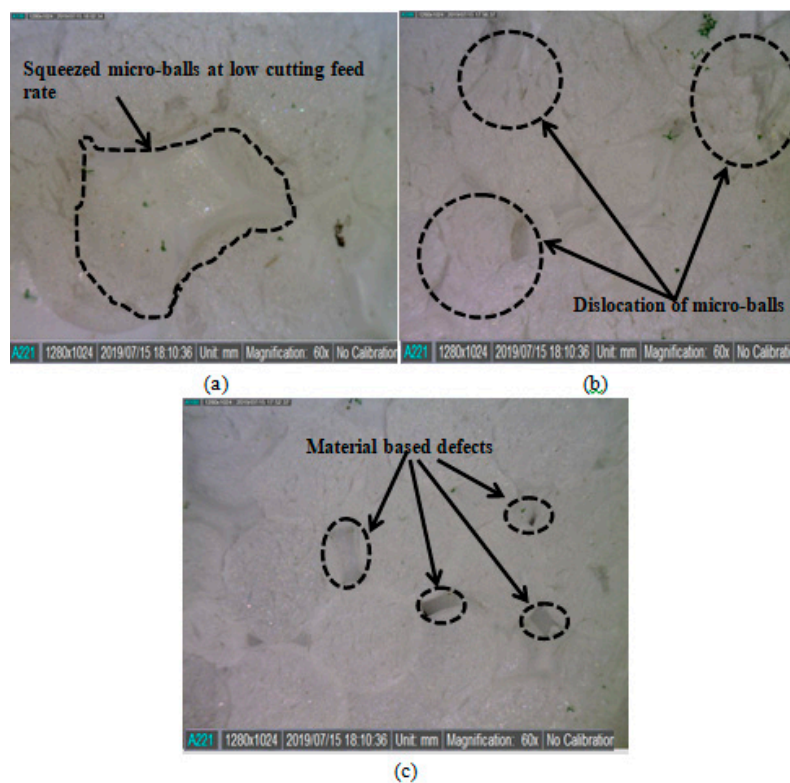


Figure 4. Surface morphology of (a) thermal squeezed (at low 30 mm), (b) dislocated (at low 30 mm), and (c) precisely machined micro-balls (at 50 mm/min).

From Figure 5, the effect of spindle speed on the DIW can be characterized. It can be seen that at 1500 rpm of spindle speed, micro-ball dislocation was observed along with the brittle fracture; refer to Figure 5a. However, when the spindle speed was increased to 1700 rpm, the brittle fracture effect was eliminated. The localized micro-ball dislocation can still be seen; refer to Figure 5b. Finally, in the case of 2000 rpm spindle speed, comparatively less dislocation of the micro-balls was observed. Since the spindle speed has affected the surface morphology of the machined EPS work material; therefore, it has influenced the dimensional accuracy. Further, in the case of depth-of-cut, it was found that the DIW of the machined EPS did not affect an increase in the cut depth from 2 to 4 mm. However, with a further addition to 6 mm, the DIW reduced. This might be because when the cut depth was 6 mm, the machined micro-balls chips were stuck within the groove and resulted in the tool tightening within the groove. In the case of DIH, it is observed from Figure 3 that the effect of input process parameters is almost similar to the DIW. This indicates that the input process parameters induced similar effects on the observed DA, both DIW and DIH. The optimized process parameters for DIW and DIH are a feed rate of 50 mm/min, a spindle speed of 2000 rpm and a depth of cut of 2 mm. Further, in the case of R_a , it is seen in Figure 3 that with an increase in the feed rate of the end-mill tool, the resulting R_a value decreases. Thus, the formation of surface unevenness is usual. The reason is similar, at low feed rate abrupt micro-ball dislocation, as well as their squeezing takes place. Further, similar effects were seen in the case of spindle speed. This means that for obtaining a finely finished machine surface, higher values of the spindle speeds are desirable. From the rendered and surface profile, refer to Figure 6: the machined surface at a feed rate of 50 mm/min, possesses surface roughness $\sim 3.04 \mu\text{m}$, whereas, in the case of 30 mm/min, the roughness is about three times higher, $\sim 9.83 \mu\text{m}$ and at low feed rate, surface irregularities are higher.

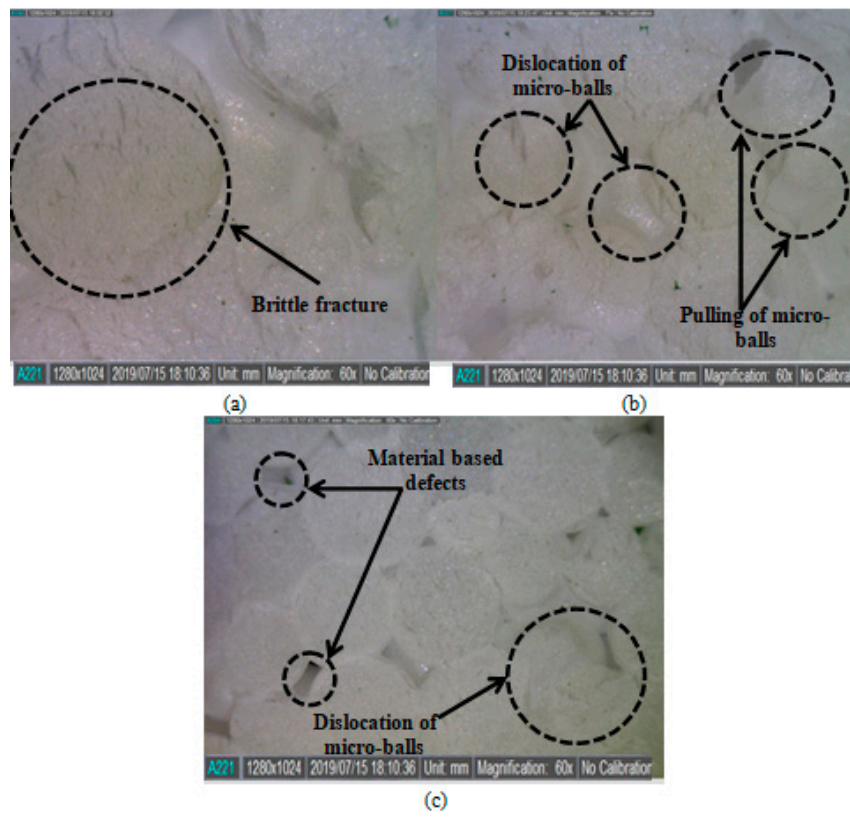


Figure 5. Surface morphology of machined EPS at (a) 1500 rpm, (b) 1700 rpm, and (c) 2000 rpm.

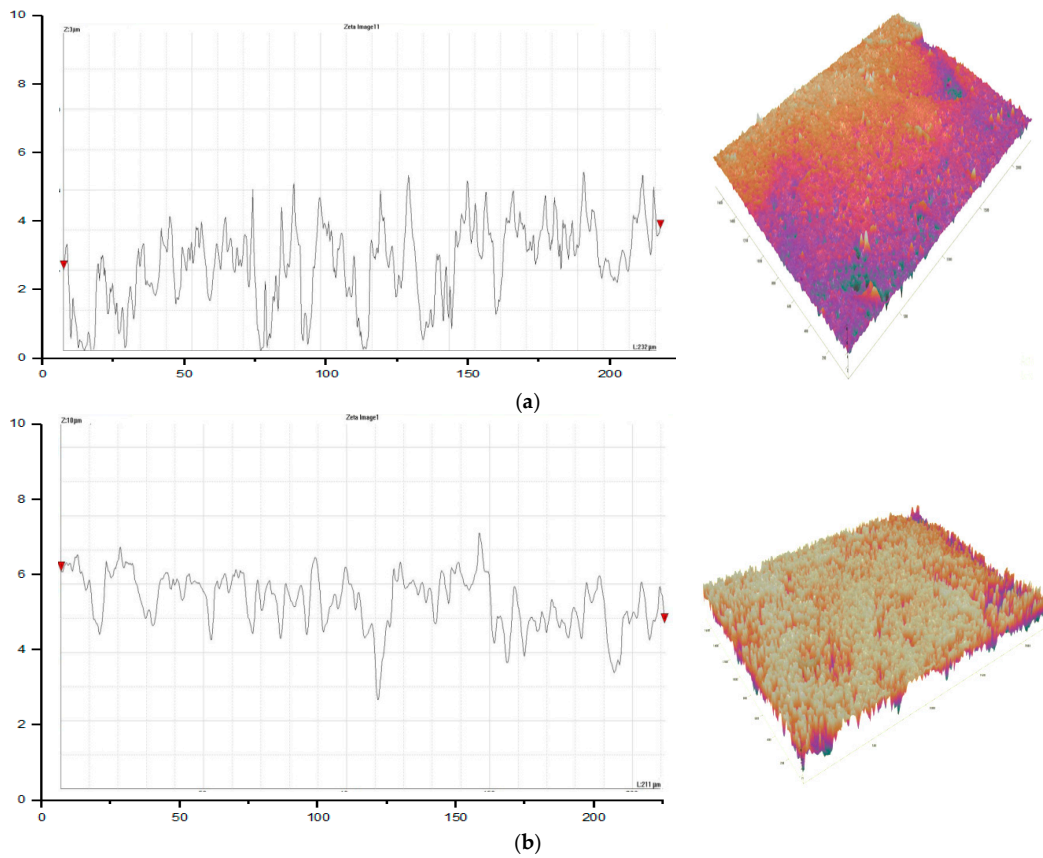


Figure 6. Cont.

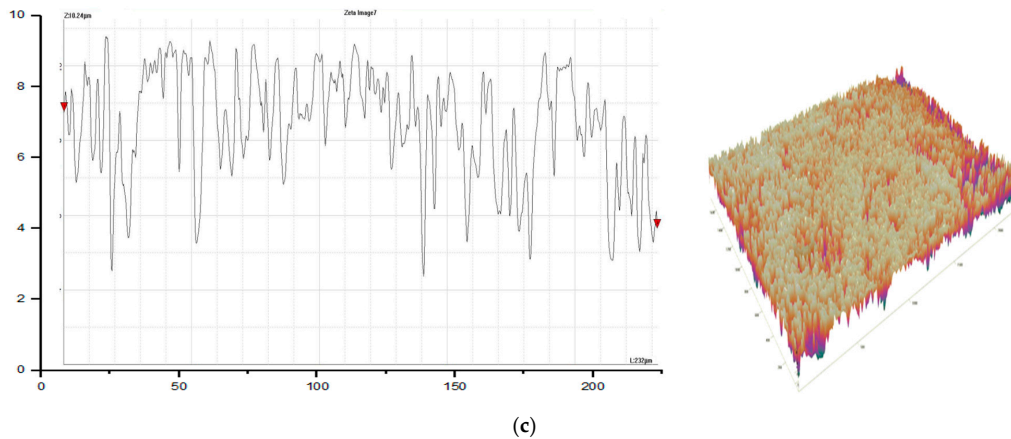


Figure 6. Surface profile and rendered surface profile: (a) 50 mm/min: $R_a \sim 3.047 \mu\text{m}$; (b) 40 mm/min: $R_a \sim 6.633 \mu\text{m}$, and (c) 30 mm/min.: $R_a \sim 9.827 \mu\text{m}$.

Moreover, From Table 5, it has been found that the percentage contribution of residual error in the case of DIW, DIH, and R_a is 2.89%, 2.43%, and 1.10%, respectively. Residual errors are lower than 5% for all responses, indicating the recording of data below the acceptable level of error. Table 6 shows the response values of the S/N ratio for the three different levels of input parameters. The values of Table 6 were used for predicting the optimized S/N ratio (β_{opt}) for DIW, DIH, and R_a by using Equation (1):

$$\beta_{opt} = \hat{m} + (\hat{m}_{1max} - \hat{m}) + (\hat{m}_{2max} - \hat{m}) + (\hat{m}_{3max} - \hat{m}), \tag{1}$$

where, \hat{m} is the overall mean of the S/N ratio (refer to Table 4), \hat{m}_{1max} , \hat{m}_{2max} , and \hat{m}_{3max} are maximum S/N ratio for 1st input parameter, 2nd input parameter, and 3rd input parameter, respectively. The values \hat{m}_{1max} , \hat{m}_{2max} , and \hat{m}_{3max} , correspond to Table 6.

Table 5. ANOVA results for DIW, DIH, and R_a .

| Source | Degree of Freedom | Sum of Square | Variance | Fisher's Value | Probability (P) | Contribution (%) |
|----------------|-------------------|---------------|----------|----------------|-----------------|------------------|
| DIW | | | | | | |
| F | 2 | 64.133 | 32.067 | 19.75 | 0.048 * | 57.01 |
| S | 2 | 40.462 | 20.231 | 12.46 | 0.074 | 35.97 |
| DoC | 2 | 4.656 | 2.328 | 1.43 | 0.411 | 4.14 |
| Residual Error | 2 | 3.248 | 1.624 | | | 2.89 |
| DIH | | | | | | |
| F | 2 | 36.302 | 18.1508 | 27.09 | 0.036 * | 65.77 |
| S | 2 | 9.465 | 4.7325 | 7.06 | 0.124 | 17.15 |
| DoC | 2 | 8.092 | 4.0459 | 6.04 | 0.142 | 14.66 |
| Residual Error | 2 | 1.34 | 0.6699 | | | 2.43 |
| R_a | | | | | | |
| F | 2 | 60.754 | 40.5863 | 30.37 | 0.013 * | 84.01 |
| S | 2 | 9.074 | 5.0431 | 4.536 | 0.081 | 12.56 |
| DoC | 2 | 1.613 | 0.6195 | 0.806 | 0.331 | 2.24 |
| Residual Error | 2 | 0.7971 | 0.6699 | | | 1.10 |

Note: * Indicates statistically significant variables.

Table 6. Delta rank of S/N responses.

| Level | F | V | DoC |
|----------------------|-----------|-----------|-----------|
| DIW | | | |
| 1 | −1.79662 | −1.66336 | 1.35969 |
| 2 | −0.03060 | 0.84546 | 1.46335 * |
| 3 | 4.53868 * | 3.52936 * | −0.11158 |
| Delta | 6.33530 | 5.19272 | 1.57493 |
| Rank | 1 | 2 | 3 |
| DIH | | | |
| 1 | −7.624 | −7.280 | −5.153 * |
| 2 | −6.849 | −5.212 | −5.175 |
| 3 | −3.029 * | −5.011 * | −7.175 |
| Delta | 4.595 | 2.269 | 2.022 |
| Rank | 1 | 2 | 3 |
| R_a | | | |
| 1 | −20.87 | −16.87 * | −17.92 |
| 2 | −19.61 | −18.13 | −17.86 * |
| 3 | −13.97 * | −19.46 | −18.68 |
| Delta | 6.91 | 2.59 | 0.82 |
| Rank | 1 | 2 | 3 |

Note: * indicates a maximum S/N ratio.

The obtained β_{opt} for DIW, DIH, and R_a is given in Equations (2)–(4):

$$\beta_{opt} = 0.904 + (4.53868 - 0.904) + (3.52936 - 0.904) + (1.46935 - 0.904) = 7.729 \text{ db}, \quad (2)$$

$$\beta_{opt} = -5.833 + (-3.029 + 5.833) + (-5.011 + 5.833) + (-5.311 + 5.833) = -1.585 \text{ db}, \quad (3)$$

$$\beta_{opt} = -18.15 + (-13.97 + 18.15) + (-16.87 + 18.15) + (-17.86 + 18.15) = -12.4 \text{ db}. \quad (4)$$

Equation (5) shows the formula to evaluate the output response from the predicted response S/N ratio and is utilized in the present work to compute responses.

$$Y_{opt}^2 = 1/10^{\beta_{opt}/10}, \quad (5)$$

where Y_{opt} is the optimal response. Furthermore, to validate the accuracy of predicting output responses, confirmation experiments ($n = 3$) were also performed at the suggested optimized parametric setting. Table 7 depicts the expected and confirmatory experiment results for the output responses. The predicted and confirmatory result shows good correlation and, therefore, validates the statistical analysis.

Table 7. Statistically predicted and confirmatory experimental values for output responses.

| Output Response | Predicted | Experimental | Deviation (\pm) |
|-------------------------|-----------|--------------|---------------------|
| DIW (mm) | 0.410 | 0.415 | 0.05 |
| DIH (mm) | 1.018 | 1.107 | 0.089 |
| R_a (μm) | 4.16 | 4.11 | 0.05 |

3.2. Tool Performance

The performance of the 3D printed tool was assessed by recording the tool wear rate. For this, the initial and final weight of the tool was measured using a digital weighing scale (accuracy 0.001 mg). It was found that despite losing weight after machining, for all the EPS samples, no weight loss was recorded. Instead of weight loss, the 3D printed ABS tool gained weight of about 0.002 mg, because of

the adhesion of the EPS machine chip on the printed tool. The material adhesion was mainly because of the heat produced at the work material, and at the 3D printed ABS tool. Figure 7 shows the pictorial view of the EPS' debris deposit on the tool. Furthermore, it was found that the ABS tool was free of any type of crack, distortion, or worn cutting edges. It was found that the 3D printed based thermoplastic machining tools are efficient in obtaining desirable quality characteristics in case of soft polymeric materials. Moreover, the wear resistance of the developed tools enables machining the soft polymers for batch and mass production runs.

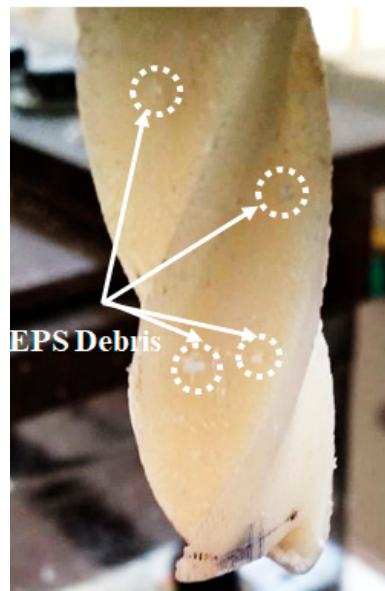


Figure 7. Pictorial view of the deposition of EPS debris on 3D printed ABS tool.

The novel applications of the 3D printing technologies to develop different types of machining tools will not only help to improve the machining efficiencies but also enable cutting-down the production times and tooling costs. In contrast, the metallic and ceramic-based 3D printing technologies can utilize harder feedstock systems to develop a cutting tool for machining different types of engineering materials. The polymer-based 3D printing technologies can use the feasibility of using ceramic or metallic reinforcements for enhancing the hardness and wear resistance of the cutting tools to the next possible level for cutting harder polymers. There have been many examples [32–35] where the reinforced 3D prints have attained improved mechanical, thermal, and wear-resistant properties. However, the potential of such feedstock systems to be used for machining polymeric materials, as well as micro-machining of comparatively harder metals and ceramic, must be explored.

In the present study, the EPS was used as the work material that exhibits much less hardness (~65 RM) and poor interatomic bonding of the pre-expanded polystyrene beads, therefore, during machining thermal shock was not seen. Furthermore, the low thermal conductivity of the EPS, ~0.034 W/mK, provided the inherent thermal-insulation to avoid any damages caused by the heat concentration during machining. However, in case of other polymeric work materials, it is essential to record the thermal images at the tool-workpiece interface in order to generate supportive knowledge.

4. Conclusions

In the current study, a novel application of a 3D printed ABS end-mill tool was explored for machining soft polymer (EPS). Based on geometrical and surface characteristics of a machined EPS, the following conclusions can be drawn.

Through scrutiny, it was found that the dimensional accuracy (of both DIW and DIH) and surface finish of the machined EPS can be improved by increasing the feed rate. From the surface morphology of the machined EPS, it was found that by increasing the feed rate machining issues of EPS, such as

thermal sensitivity and material dislocation can be controlled. Furthermore, it was found that at a higher level of spindle speed, the dimensional accuracy and surface finish of the machined EPS improved. This is because, at a lower level of the spindle speed, the cutting mechanism included micro-balls dislocation followed by brittle fracture. However, in the case of depth-of-cut, the optimized level corresponding to dimensional accuracy and surface finish is 2 mm. The optimized process parametric levels, in regard to dimensional accuracy and surface roughness, have been obtained and verified statically through ANOVA. It was found that the feed rate is the only statistically significant process parameter for all output responses. Along with this, the predicted optimized parametric levels and S/N ratios were verified through confirmatory experiments, where a strong correlation was found between the predicted and experimental values.

The performance analysis of the 3D printed ABS tool highlighted that the developed tool is capable of machining soft polymers with controlled dimensional and topographic features. Furthermore, investigations should explore the potential of the reinforced 3D printed tool for machining tough and harder polymers.

Author Contributions: K.S., G.S., and S.S.: performed the experimentations. G.S., C.P., R.K., and C.I.P.: performed the data analysis. S.S., G.S., G.K., and S.R.: conducted the characterization. K.S., S.S., C.I.P., and R.K.: wrote the draft of the manuscript. G.K., and R.K.: reviewed the draft and pointed out the shortcomings. S.S., C.P., R.K. and C.I.P.: revised the manuscript. All authors have read and agreed to the published version of the manuscript.

Funding: This research received no external funding.

Acknowledgments: Sunpreet Singh would like to acknowledge the technical support provided by Rupinder Singh of Mechanical Engineering, NITTTR, Chandigarh (India) and technical staff members of MRL Laboratory, Production Engineering, Guru Nanak Dev Engineering College (India).

Conflicts of Interest: There is no conflict of interest.

References

- Dick, J.; Hull, E.; Jackson, K. *Requirements Engineering*; Springer: Basel, Switzerland, 2017.
- Duflou, J.R.; Sutherland, J.W.; Dornfeld, D.; Herrmann, C.; Jeswiet, J.; Kara, S.; Hauschild, M.; Kellens, K. Towards energy and resource efficient manufacturing: A processes and systems approach. *CIRP Ann.* **2012**, *61*, 587–609. [[CrossRef](#)]
- Chen, D.; Heyer, S.; Ibbotson, S.; Salonitis, K.; Steingrímsson, J.G.; Thiede, S. Direct digital manufacturing: Definition, evolution, and sustainability implications. *J. Clean. Prod.* **2015**, *107*, 615–625. [[CrossRef](#)]
- Bradley, R.; Jawahir, I.S.; Badurdeen, F.; Rouch, K. A framework for material selection in multi-generational components: Sustainable value creation for a circular economy. *Procedia CIRP* **2016**, *48*, 370–375. [[CrossRef](#)]
- Kellens, K.; Mertens, R.; Paraskevas, D.; Dewulf, W.; Duflou, J.R. Environmental Impact of Additive Manufacturing Processes: Does AM contribute to a more sustainable way of part manufacturing? *Procedia CIRP* **2017**, *61*, 582–587. [[CrossRef](#)]
- Huang, S.H.; Liu, P.; Mokasdar, A.; Hou, L. Additive manufacturing and its societal impact: A literature review. *Int. J. Adv. Manuf. Technol.* **2013**, *67*, 1191–1203. [[CrossRef](#)]
- Balogun, V.A.; Kirkwood, N.; Mativenga, P.T. Energy consumption and carbon footprint analysis of Fused Deposition Modelling: A case study of RP Stratasy's Dimension SST FDM. *Int. J. Sci. Eng. Res.* **2015**, *6*, 1–6.
- Freitas, D.; Almeida, H.A.; Bártolo, H.; Bártolo, P.J. Sustainability in extrusion-based additive manufacturing technologies. *Prog. Addit. Manuf.* **2016**, *1*, 65–78. [[CrossRef](#)]
- Turner, B.N.; Gold, S.A. A review of melt extrusion additive manufacturing processes: II. Materials, dimensional accuracy, and surface roughness. *Rapid Prototyp. J.* **2015**, *21*, 250–261. [[CrossRef](#)]
- Cicala, G.; Latteri, A.; Del Curto, B.; Lo Russo, A.; Recca, G.; Farè, S. Engineering thermoplastics for additive manufacturing: A critical perspective with experimental evidence to support functional applications. *J. Appl. Biomater. Funct. Mater.* **2017**, *15*, 10–18. [[CrossRef](#)]
- Suárez, L.; Domínguez, M. Sustainability and environmental impact of fused deposition modelling (FDM) technologies. *Int. J. Adv. Manuf. Technol.* **2020**, *106*, 1267–1279. [[CrossRef](#)]
- Wohlers, T.T. *Wohlers Report 2011: Additive Manufacturing and 3D Printing State of the Industry Annual Worldwide Progress Report*; Wohlers Associates Inc.: Fort Collins, CO, USA, 2011.

13. Anitha, R.; Arunachalam, S.; Radhakrishnan, P. Critical parameters influencing the quality of prototypes in fused deposition modelling. *J. Mater. Process. Technol.* **2001**, *118*, 385–388. [[CrossRef](#)]
14. Sood, A.K.; Ohdar, R.K.; Mahapatra, S.S. Parametric appraisal of mechanical property of fused deposition modelling processed parts. *Mater. Des.* **2010**, *31*, 287–295. [[CrossRef](#)]
15. Harris, M.; Potgieter, J.; Archer, R.; Arif, K.M. In-process thermal treatment of polylactic acid in fused deposition modelling. *Mater. Manuf. Process.* **2019**, *34*, 701–713. [[CrossRef](#)]
16. Brooks, H.; Rennie, A.; Abram, T.; McGovern, J.; Caron, F. Variable fused deposition modelling: Analysis of benefits, concept design and tool path generation. In Proceedings of the 5th International Conference on Advanced Research in Virtual and Rapid Prototyping, Leiria, Portugal, 28 September–1 October 2011; pp. 511–517.
17. Lužanin, O.; Movrin, D.; Plančak, M. Effect of layer thickness, deposition angle, and infill on maximum flexural force in FDM-built specimens. *J. Technol. Plast.* **2014**, *39*, 49–58.
18. Giri, J.; Patil, A.; Prabhu, H. The Effect of Various Parameters on the Nozzle Diameter and 3D Printed Product in Fused Deposition Modelling: An Approach. In *Proceedings of 2nd International Conference on Communication, Computing and Networking*; Springer: Singapore, 2019; pp. 839–847. [[CrossRef](#)]
19. uzZaman, U.K.; Boesch, E.; Siadat, A.; Rivette, M.; Baqai, A.A. Impact of fused deposition modeling (FDM) process parameters on strength of built parts using Taguchi's design of experiments. *Int. J. Adv. Manuf. Technol.* **2019**, *101*, 1215–1226.
20. El Magri, A.; El Mabrouk, K.; Vaudreuil, S.; EbnTouhami, M. Mechanical properties of CF-reinforced PLA parts manufactured by fused deposition modeling. *J. Thermoplast. Compos. Mater.* **2019**, *12*, 0892705719847244. [[CrossRef](#)]
21. Bikas, H.; Lianos, A.K.; Stavropoulos, P. A design framework for additive manufacturing. *Int. J. Adv. Manuf. Technol.* **2019**, *106*, 3769–3783. [[CrossRef](#)]
22. Samykano, M.; Selvamani, S.K.; Kadirgama, K.; Ngui, W.K.; Kanagaraj, G.; Sudhakar, K. Mechanical property of FDM printed ABS: Influence of printing parameters. *Int. J. Adv. Manuf. Technol.* **2019**, *102*, 2779–2796. [[CrossRef](#)]
23. Singh, S.; Singh, N.; Gupta, M.; Prakash, C.; Singh, R. Mechanical feasibility of ABS/HIPS-based multi-material structures primed by low-cost polymer printer. *Rapid Prototyp. J.* **2019**, *25*, 152–161. [[CrossRef](#)]
24. Naresh, K.; Jayaganthan, R.; Velmurugan, R. A comparative study between in-house 3D printed and injection molded ABS and PLA polymers for low-frequency applications. *Mater. Res. Express* **2019**, *6*, 085345.
25. Singh, S.; Prakash, C.; Antil, P.; Singh, R.; Królczyk, G.; Pruncu, C.I. Dimensionless Analysis for Investigating the Quality Characteristics of Aluminium Matrix Composites Prepared through Fused Deposition Modelling Assisted Investment Casting. *Materials* **2019**, *12*, 1907. [[CrossRef](#)]
26. Harris, M.; Potgieter, J.; Archer, R.; Arif, K.M. Effect of Material and Process Specific Factors on the Strength of Printed Parts in Fused Filament Fabrication: A Review of Recent Developments. *Materials* **2019**, *12*, 1664. [[CrossRef](#)] [[PubMed](#)]
27. Waheed, S.; Cabot, J.M.; Smejkal, P.; Farajikhah, S.; Sayyar, S.; Innis, P.C.; Beirne, S.; Barnsley, G.; Lewis, T.W.; Breadmore, M.C.; et al. 3D printing of abrasive, hard and thermally conductive synthetic micro-diamond-polymer composite using low-cost fused deposition modelling printer. *ACS Appl. Mater. Interfaces* **2019**, *11*, 4353–4363. [[CrossRef](#)] [[PubMed](#)]
28. Corcione, C.E.; Gervaso, F.; Scalera, F.; Padmanabhan, S.K.; Madaghiele, M.; Montagna, F.; Sannino, A.; Licciulli, A.; Maffezzoli, A. Highly loaded hydroxyapatite microsphere/PLA porous scaffolds obtained by fused deposition modelling. *Ceram. Int.* **2019**, *45*, 2803–2810. [[CrossRef](#)]
29. Nikzad, M.; Masood, S.H.; Sbarski, I. Thermo-mechanical properties of a highly filled polymeric composites for fused deposition modeling. *Mater. Des.* **2011**, *32*, 3448–3456. [[CrossRef](#)]
30. Grimm, T. Fused deposition modeling: A technology evaluation. *Time-Compress. Technol.* **2003**, *11*, 1–6.
31. Ho, C.M.; Ng, S.H.; Li, K.H.; Yoon, Y.J. 3D printed microfluidics for biological applications. *Lab Chip* **2015**, *15*, 3627–3637. [[CrossRef](#)]
32. Hierl, T.; Arnold, S.; Kruber, D.; Schulze, F.P.; Hümpfner-Hierl, H. CAD-CAM-Assisted Esthetic Facial Surgery. *J. Oral Maxillofac. Surg.* **2013**, *71*, 15–23. [[CrossRef](#)]
33. Kumta, S.; Kumta, M.; Jain, L.; Purohit, S.; Ummul, R. A novel 3D template for mandible and maxilla reconstruction: Rapid prototyping using stereolithography. *Indian J. Plastic Surg. Off. Publ. Assoc. Plast. Surg. India* **2015**, *48*, 263. [[CrossRef](#)]

34. Ciocca, L.; De Crescenzo, F.; Fantini, M.; Scotti, R. CAD/CAM and rapid prototyped scaffold construction for bone regenerative medicine and surgical transfer of virtual planning: A pilot study. *Comput. Med. Imaging Graph.* **2009**, *33*, 58–62. [[CrossRef](#)]
35. Masood, S.H.; Song, W.Q. Development of new metal/polymer materials for rapid tooling using fused deposition modelling. *Mater. Des.* **2004**, *25*, 587–594. [[CrossRef](#)]
36. Attivissimo, F.; Lanzolla, A.M.; Carlone, S.; Larizza, P.; Brunetti, G. TDM-FDM configuration of electromagnetic tracking system for image-guided surgery devices. In Proceedings of the 2017 IEEE International Instrumentation and Measurement Technology Conference (I2MTC), Turin, Italy, 22–25 May 2017; pp. 1–6.
37. Chen, H.; Yang, X.; Chen, L.; Wang, Y.; Sun, Y. Application of FDM three-dimensional printing technology in the digital manufacture of custom edentulous mandible trays. *Sci. Rep.* **2016**, *14*, 19207. [[CrossRef](#)] [[PubMed](#)]
38. Singh, N.; Singh, R.; Ahuja, I.P. On Development of Functionally Graded Material Through Fused Deposition Modelling Assisted Investment Casting from Al₂O₃/SiC Reinforced Waste Low Density Polyethylene. *Trans. Indian Inst. Met.* **2018**, *71*, 2479–2485. [[CrossRef](#)]
39. Singh, R.; Singh, S.; Fraternali, F. Development of in-house composite wire based feed stock filaments of fused deposition modelling for wear-resistant materials and structures. *Compos. Part B Eng.* **2016**, *98*, 244–249. [[CrossRef](#)]
40. McCullough, E.J.; Yadavalli, V.K. Surface modification of fused deposition modeling ABS to enable rapid prototyping of biomedical microdevices. *J. Mater. Process. Technol.* **2013**, *213*, 947–954. [[CrossRef](#)]
41. Mohammed, M.; Fitzpatrick, A.; Malyala, S.; Gibson, I. Customised design and development of patient specific 3D printed whole mandible implant. In Proceedings of the 27th Annual International Solid Freeform Fabrication Symposium, Austin, TX, USA, 8–10 August 2016; pp. 1708–1717.
42. Tsouknidas, A.; Pantazopoulos, M.; Katsoulis, I.; Fasnakis, D.; Maropoulos, S.; Michailidis, N. Impact absorption capacity of 3D-printed components fabricated by fused deposition modelling. *Mater. Des.* **2016**, *102*, 41–44. [[CrossRef](#)]
43. Mohamed, O.; Masood, S.; Bhowmik, J. Analytical modelling and optimization of the temperature-dependent dynamic mechanical properties of fused deposition fabricated parts made of PC-ABS. *Materials* **2016**, *9*, 895. [[CrossRef](#)] [[PubMed](#)]
44. Skowrya, J.; Pietrzak, K.; Alhnan, M.A. Fabrication of extended-release patient-tailored prednisolone tablets via fused deposition modelling (FDM) 3D printing. *Eur. J. Pharm. Sci.* **2015**, *68*, 11–17. [[CrossRef](#)]
45. Hong, C.; Yuan, Y.; Yang, Y.; Zhang, Y.; Abro, Z.A. A simple FBG pressure sensor fabricated using fused deposition modelling process. *Sens. Actuators A: Phys.* **2019**, *285*, 269–274. [[CrossRef](#)]
46. Durgun, I. Sheet metal forming using FDM rapid prototype tool. *Rapid Prototyp. J.* **2015**, *21*, 412–422. [[CrossRef](#)]
47. Haerberle, G.; Desai, S. Investigating Rapid Thermoform Tooling Via Additive Manufacturing (3d Printing). *Am. J. Appl. Sci.* **2019**, *16*, 238–243. [[CrossRef](#)]
48. Malak, S.F.; Anderson, I.A. Orthogonal of polyurethane foam. *Int. J. Mech. Sci.* **2005**, *47*, 867–883. [[CrossRef](#)]
49. Sood, A.K.; Ohdar, R.K.; Mahapatra, S.S. Improving dimensional accuracy of fused deposition modelling processed part using grey Taguchi method. *Mater. Des.* **2009**, *30*, 4243–4252. [[CrossRef](#)]
50. Fernandez-Vicente, M.; Calle, W.; Ferrandiz, S.; Conejero, A. Effect of infill parameters on tensile mechanical behavior in desktop 3D printing. *3D Print. Addit. Manuf.* **2016**, *3*, 183–192. [[CrossRef](#)]
51. Jouaneh, M.; Hammad, A.; Datsaris, P. A flexible automated foam cutting system. *Int. J. Mach. Tools Manuf.* **1997**, *37*, 437–449. [[CrossRef](#)]
52. Brooks, H.; Aitchison, D. A review of state-of-the-art large-sized foam cutting rapid prototyping and manufacturing technologies. *Rapid Prototyp. J.* **2010**, *16*, 318–327. [[CrossRef](#)]
53. Da Silva, F.P.; Beretta, E.M.; Prestes, R.C.; Junior, W.K. Design and milling manufacture of polyurethane custom contoured cushions for wheelchair users. *Australas. Med J.* **2011**, *4*, 500. [[CrossRef](#)]
54. Ahn, D.G.; Lee, S.H.; Yang, D.Y. A study on the influence of the sloped cutting angle on kerfwidth and part quality in the hotwire cutting of EPS foam for the VLM-s rapid prototyping process. *Int. J. Mach. Tools Manuf.* **2003**, *43*, 1447–1464. [[CrossRef](#)]
55. Shim, V.; Boheme, J.; Josten, C.; Anderson, I. Use of polyurethane foam in orthopaedic biomechanical experimentation and simulation. *Polyurethane* **2012**. [[CrossRef](#)]

56. Lanz, R.W.; Melkote, S.N.; Kotnis, M. Effect of process parameters and tool shape on the machinability of a particulate filled-polymer composite material for rapid tooling. *Mach. Sci. Technol.* **2001**, *5*, 217–237. [[CrossRef](#)]
57. Azmi, A.I.; Lin, R.J.; Bhattacharyya, D. Machinability study of glass fibre-reinforced polymer composites during end milling. *Int. J. Adv. Manuf. Technol.* **2013**, *64*, 247–261. [[CrossRef](#)]
58. Kacker, R.N.; Lagergren, E.S.; Filliben, J.J. Taguchi's orthogonal arrays are classical designs of experiments. *J. Res. Natl. Inst. Stand. Technol.* **1991**, *96*, 577. [[CrossRef](#)] [[PubMed](#)]



© 2020 by the authors. Licensee MDPI, Basel, Switzerland. This article is an open access article distributed under the terms and conditions of the Creative Commons Attribution (CC BY) license (<http://creativecommons.org/licenses/by/4.0/>).